# Eastern USA summer temperatures since 1461 CE show connections to volcanic forcing and jet stream dynamics

**Grant Harley**

gharley@uidaho.edu

University of Idaho College of Science https://orcid.org/0000-0003-1557-8465

**Justin Maxwell**

Indiana University Bloomington

**Karen King**

The University of Tennessee Knoxville

**Shelly Rayback**

University of Vermont

**Edward Cook**

Columbia University Lamont-Doherty Earth Observatory: Lamont-Doherty Earth Observatory

**Christopher Hansen**

University of Vermont

**Richard Stockton Maxwell**

Radford University

**Frederick Reinig**

Johannes Gutenberg University: Johannes Gutenberg Universitat Mainz

**Jan Esper**

Johannes Gutenberg University: Johannes Gutenberg Universitat Mainz

**Tsun Fung Au**

University of Michigan

**Ellen Bergan**

University of Idaho

**Katherine Brings**

University of Idaho

**Nick Koenig**

University of Idaho

**Benjamin Lockwood**

Penn State University: The Pennsylvania State University

**Richard Thaxton**

University of Idaho

**Research Article**

**Keywords:**

**Posted Date:** March 13th, 2024

**DOI:** https://doi.org/10.21203/rs.3.rs-4015457/v1



**Version of Record:** A version of this preprint was published at Climatic Change on September 5th, 2024. See the published version at https://doi.org/10.1007/s10584-024-03798-z.

# Eastern USA summer temperatures since 1461 CE show connections to volcanic forcing and jet stream dynamics

Received: date / Accepted: date

**Abstract** Contextualizing current increases in Northern Hemisphere temperatures is precluded by the short instrumental record of the past *ca.* 120 years and the dearth of temperature-sensitive proxy records, particularly at lower latitudes south of <50 °N. We develop a network of 29 blue intensity chronologies derived from tree rings of *Tsuga canadensis* (L.) Carrière and *Picea rubens* Sarg. trees distributed across the Mid-Atlantic and Northeast USA (MANE)—a region underrepresented by multi-centennial temperature records. We use this network to reconstruct March-September air temperatures back to 1461 CE based on a model that explains 62% of the instrumental temperature variance from 1901−1976 CE. Since 1998 CE, MANE summer temperatures are consistently the warmest within the context of the past 561 years exceeding the 1951−1980 mean +1.3 °C. Temperature variability across MANE is linked with the position and intensity of the Northern Hemisphere polar jet stream (NHJ), which triggers regional warm and cool extremes, respectively. The new network reveals a strong regional temperature response to large volcanic eruptions, with the most severe temperature departure of -1.05 °C following the eruption of Mount Tambora in 1815 CE. Expanding the MANE network to the west and south and combining it with existing temperature-sensitive proxies across North America is an important next step toward producing a gridded temperature reconstruction field for North America.

## 1 Introduction

Over the 20$^{\text{th}}$ century, annual surface air temperatures in the eastern United States (US) have risen by more than 1 °C and are projected to continue increasing throughout this century (Kunkel et al., 2013; Horton et al., 2014; Vose et al., 2017). In parallel with rising temperatures across eastern North America, temperatures have also increased by approximately 4°C across the adjacent Arctic (Rantanen et al., 2022) due to the Arctic Amplification effect. The Arctic Amplification is thought to destabilize atmospheric dynamics including the position of the tropospheric Northern Hemisphere polar jet stream (NHJ) which impacts

Address(es) of author(s) should be given

both temperature and precipitation regimes in the eastern US in various ways across seasons (Belmecheri et al., 2017). Changes in the NHJ position along with the development of stronger trough and ridge pressure gradients could also be directly impacting extreme weather regimes in the eastern US (Francis et al., 2009; Francis and Vavrus, 2015; Overland et al., 2015). As such, mean annual temperature across the Mid-Atlantic to Northeast region of the US (hereafter MANE) has increased approximately 2 °C since 1960 (Vose et al., 2017). While the last 100 years of instrumental climate data are valuable for understanding the current temperature trends, a long-term perspective of temperature variability is essential to understanding the associated drivers in addition to recent anthropogenic climate effects, specifically before the Industrial Revolution. To overcome this issue, paleoclimate proxy data, such as tree rings, can be applied to gain high-resolution insights into climate variability before the instrumental period (*ca.* 1900).

Reconstruction of climate variability, particularly temperature, in the eastern US has been challenging due to the land-use history and ecology of eastern forests which leaves few old trees on the landscape with which to build proxy records. In the eastern US, there are three primary tree species known to exhibit sensitivity to temperature: *Chamaecyparis thyoides* L. (Atlantic white cedar), *Tsuga canadensis*(L.) Carrière (eastern hemlock), and *Picea rubens* Sarg. (red spruce). *C. thyoides* for instance, displays a temperature signal extending from winter to summer (Pederson et al., 2004; Hopton and Pederson, 2005). Pearl et al. (2017) developed a mean January-August temperature reconstruction for the northeast US based on *C. thyoides* ring-width chronologies that explained 34% of the instrumental variance. By increasing the number of sites, Pearl et al. (2020b) expanded on their earlier efforts and produced a more robust spatial temperature field reconstruction for New England, but the temperature record, based exclusively on *C. thyoides*, only extends to the *ca.* 1820s. *T. canadensis*, on the other hand, has been shown to contain a strong prior- and current-year temperature signal and is a broadly distributed, low elevation (*e.g.* <400 m), and long-lived (>400 years) species in eastern North America (Cook and Cole, 1991; Tardif et al., 2001; Maxwell et al., 2020; Stern et al., 2021; Harley et al., 2021). Finally, *P. rubens* is a shade-tolerant conifer that can live for more than 300 years. Previous studies show *P. rubens* from the Northeast US to be sensitive to spring (Apr−May) temperature variability (Conkey, 1986; Sheppard et al., 1996; Kosiba et al., 2018). The core distribution of *P. rubens* is in northeastern US and Canada but is also found in small, disjunct populations in the southern Appalachian Mountains of eastern Tennessee, western North Carolina, and northern Georgia. The so-called *spruce zone*—where *P. rubens* attains its maximum importance as a primary producer in the spruce-fir community—varies across its geographic range by elevation, with individuals positioned within a wider elevation envelop in the northern part of its range <650–>950 m asl (Foster and D'Amato, 2015; Kosiba et al., 2018), but only found at elevations >1400 m asl at southern range margins (McLaughlin et al., 1987).

A concerted effort has been made over the past few decades to establish a network of high-resolution temperature proxy records throughout the Northern Hemisphere to gauge temperature variability (Esper et al., 2002; Frank et al., 2007; Wilson et al., 2007; Jones et al., 1998; Mann et al., 1999, 2009; Wahl and Ammann, 2007). With the recent formation of the Northern Hemisphere Tree-Ring Network Development (N-TREND), this consortium aims to define a collective strategy for improving large-scale summer temperature reconstructions from new and existing tree-ring chronologies (Wilson et al., 2016). Currently, most N-TREND records are located at higher latitudes (>50 °N), thus, substantial spatial gaps exist in the North American region of the N-TREND network (Anchukaitis et al., 2017). In particular, the MANE region is underrepresented due to a lack of temperature-sensitive tree-ring records. Since the creation of the N-TREND network, advances in dendrochronological techniques such as blue intensity (McCarroll et al., 2002) have demonstrated the ability to provide robust paleotemperature estimates at the mid-to-lower latitudes across many regions of the Northern Hemisphere (Heeter et al., 2019, 2020, 2021; Cao et al., 2022; Zheng et al., 2023). In North America, recent work (Wang et al., 2022; Harley et al., 2021) has demonstrated the promising potential of using BI methods to improve the spatial gaps in the North American paleotemperature record over the eastern US and Canada.

As rising temperatures and heat waves increase stress on natural and human systems, particularly in a region of the US where >72 million people live, a better understanding of the historical context of current summer warmth in the eastern US requires more accurate estimations of past trends and drivers of summer temperatures. Building upon the work of Harley et al. (2021), we expand and evaluate the pre-existing network of latewood blue intensity (LWBI) data from *T. canadensis* and *P. rubens* trees to develop a regional-scale reconstruction of summer temperatures for the MANE region of the US. Using this network, we addressed the following research questions: [1] Is the rate of warming across the MANE region since *ca.* 1960 unprecedented within the context of the past *ca.* 500 years? [2] What is the full range of pre-instrumental temperature variability for MANE? [3] What are the natural and anthropogenic forcings on temperature over the last *ca.* 500 years?

## 2 Data and Methods

### 2.1 Tree-ring Network

Spanning a latitudinal range from Maryland to Maine (Figure 1), tree-ring data for the reconstruction are sourced from two conifer species in the eastern US that are suitable for BI (Heeter et al., 2019; Harley et al., 2021): *T. canadensis* and *P. rubens*. First, the majority of the MANE LWBI network is comprised of preexisting *T. canadensis* samples collected during the 1970s and 1980s by Cook and Cole (1991), who targeted the oldest known stands across much of the species' range in the US. Many of these site collections from the original study have since succumbed to logging or other disturbances (*e.g.* physical, biological); hence, the physical cores from these collections are arguably priceless within the context of this study and broader dendrochronological archives. In October 2020, we obtained the original collections from the wood archive at Columbia University's Lamont-Doherty Earth Observatory Tree-Ring Lab. We selected collections with the greatest length and sample replication back in time, specifically targeting collections that extended before 1600 CE. Further making use of preexisting collections, we obtained physical samples cored in 2012−2013 by Belmecheri et al. (2021), which comprised multiple recollections of the same sites cored in the 1970s and 1980s by Cook and Cole (1991), as well as new site collections.

Supplementing the reprocessing of existing collections for BI, we conducted a series of additional recollections during the summers spanning 2019−2021 at several of the Cook and Cole (1991) and Belmecheri et al. (2021) sites, as well as collected two new sites (Swallow Falls, Maryland and Nancy Brook, New Hampshire) in summer 2021. At each of the 2019−2021 new and recollection sites, we gathered two cores from 20−30 trees with handheld increment borers. Tree cores were prepared following protocol detailed by Harley et al. (2021). For all preexisting collections, all physical samples were re-sanded, scanned, measured, and visually crossdated using the same procedure detailed above. For each site, we measured total ring width using the CooRecorder program (Larsson, 2014). We statistically validated visual crossdating for all site collections using the total ring width series and the xDater Shiny application (Bunn, 2008, 2010). Once each site collection was absolutely dated, we collected LWBI from all samples in CooRecorder. For each site, we used the RCSigFree program (https://www.geog.cam.ac.uk/research/projects/dendrosoftware/) to standardize all tree-ring series using the signal-free standardization (Melvin and Briffa, 2008) in which the base curve was a smoothing spline with an amplitude response of 0.50 at a period associated with 67% of each series length (Cook and Peters, 1981). This method was chosen to retain as much climate signal as possible while removing non-climatic signal related to disturbance and age-related tree-ring growth trends. To account for the effect of diminishing sample size back through time, we applied variance stabilization during the standardization process and then truncated each chronology where the expressed population signal statistic fell below a threshold of 0.80 (Wigley et al., 1984; Maxwell et al., 2017).

## 2.2 Instrumental Temperature Data

We relied on previous results from Harley et al. (2021) in which the association between instrumental temperature and site LWBI chronologies at five *T. canadensis* and one *P. rubens* sites (all of which are included in this study) and found mean temperatures from March-October ($T_{\text{Mar-Oct}}$) to be the most robust predictor of LWBI variability. A principal components analysis (PCA) amongst all sites revealed PC1 to account for 39% of the cumulative proportion of variance. We noticed that including $T_{\text{Oct}}$ resulted in weaker associations contrary to Harley et al. (2021); $T_{\text{Mar-Sep}}$ resulted in the strongest predictor of $PC_1$ (Figure 2). We used $PC_1$ to identify the climatic footprint of the network by conducting a spatial Pearson's correlation between $PC_1$ and the CRU TS4.07 monthly mean air temperature field (Harris et al., 2020) during the period 1901−1976, the common period of overlap amongst all sites. Mapping the area of highest correlation ($r$=0.6+, $p<0.05$) space between $PC_1$ and the gridded spatial temperature field revealed a broad climate footprint across the eastern US (Mid-Atlantic, Northeast, and Midwest) and south-eastern Canada (Figure S6). However, given the lack of predictor BI chronologies from the Midwest US and south-eastern Canada, we elected to be more conservative with our target instrumental temperature data. Thus, we averaged $T_{\text{Mar-Sep}}$ data from the CRU TS4.07 field within the vicinity of our predictor chronologies across the MANE region (hatched area in Figure 1).

## 2.3 Reconstruction Model

We reconstructed estimates of regionalized summer air temperature using a nested principal components regression (PCR) model, which accounts for the decrease in the number of predictor chronologies back through time (Cook et al., 1999, 2004, 2007). During the initial screening phase, we prewhitened both the LWBI predictors and instrumental data to ensure independence before modeling to meet the assumptions of normality (Cook and Peters, 1997). LWBI chronologies from the initial candidate pool were retained for PCR modeling if they contained positive and significant correlations ($p<0.10$ for Pearson's, Spearman, and Robust Pearson's tests) with the predictand data over the common period of overlap amongst all predictors in the candidate pool (1901-1976). Following the Kaiser-Guttman rule (Guttman, 1954; Kaiser, 1960), the first $n$ eigenvectors with eigenvalues $>1$ were retained for the multiple regression. The final subset of PCs in the regression model was determined by considering the minimum Akaike information criterion (AIC), which includes a penalty term for increasing the number of predictors in the model (Akaike, 1974). The first model was calibrated for the common period of all chronologies (1901-1976) with the target instrumental data. Successive models were calculated backward in time intervals based on chronology length, with fewer chronologies as they dropped out. Similarly, forward nests were calculated in intervals based on when the most recent chronologies ended to include more recent tree-ring collections.

To validate each backward- and forward-nested reconstruction model, we split the common period (1901−1976) into two equal periods for calibration (1939−1976) and verification (1901−1938). To ensure each model was time stable, we calculated validation statistics for models calibrated on the "late" period (1939−1976) and verified on the "early" period (1901−1938), as well as flipped to calibrate on the early and verify on the late. We performed model validation by calculating two goodness-of-fit tests: the reduction of error (RE) and coefficient of efficiency (CE) (Fritts, 1976; Cook et al., 1999). The validation statistics produced were the calibration and verification period coefficient of determination and the verification period reduction of error and coefficient of efficiency. We produced the final reconstruction by calibrating on the full common period. After each nest was calculated, temperature estimates along with each set of calibration and verification statistics were spliced together for the entire reconstruction length. Finally, we used the methods of Robeson et al. (2020) to bias-correct the reconstruction to the target instrumental data using a quantile mapping approach based on localized linear regression (Figure S1).

## 2.4 Reconstruction Assessment

We characterize past temperature variability using a severity-duration analysis (González and Valdés, 2003) of reconstructed $T_{\text{Mar-Sep}}$ values. This analysis quantifies the magnitude (average cumulative departure from the long-term mean), duration (period of each event), and intensity (duration divided by the magnitude) of anomalously warm and cool events. Here, we considered an 'event' to be any warm or cool period spanning at least two consecutive years. We used a superposed epoch analysis (SEA; $p<0.05$) to investigate the influence of large-scale volcanic eruptions on MANE warm-season temperatures. For the event list, we used the largest volcanic eruption years based on estimated aerosol optical depth from 1461-1900 (n=8) (Toohey and Sigl, 2017), as well as the instrumental-period eruptions of 1912 (Novarupta), 1963 (Agung), 1982 (El Chicon), and 1991 (Pinatubo). To better understand linkages with upper-level atmospheric dynamics, we compared our temperature reconstruction to the position of the NHJ using a SEA ($p<0.05$). This was done by considering years during which extreme northern and southern latitudinal positions (exceeding ±1 SD as calculated from the 1725−2000 mean) of the NHJ reconstruction from Trouet et al. (2018) to use as the event list for the SEA against our temperature reconstruction. Last, we performed spatial field correlations between the temperature reconstruction and the following gridded products: 300-hpa zonal and meridional wind stress (Compo et al., 2011) and 500-hpa geopotential height from 20$^{\text{th}}$ Century Reanalysis V3 during the period 1836−2021 (Compo et al., 2011), and instrumental sea surface temperature from HadISST 1°reconstruction during the period 1870−2021 (Rayner et al., 2003).

## 3 Results and Discussion

### 3.1 MANE BI network

We developed 29 LWBI chronologies across the MANE region, all of which were used as predictors in the $T_{\text{Mar-Sep}}$ reconstruction (Figure 1AB; Table S1). Of the 29 records, 28 derive from *T. canadensis* and one from *P. rubens*. LWBI predictor chronology strength varies in the reconstruction model from $r$=0.28 (Salt Springs State Park, PA) to $r$=0.68 (Alander Mountain, MA) over the 1901−1976 period ($p<0.10$). The 28 chronologies included in the reconstruction did not vary substantially in elevation (Harley et al., 2021), but they did vary by latitude. However, results show a non-linear relationship found between latitude and each site $PC_1$ loading (Figure S2). We attribute this non-linear relationship to microclimate site characteristics of *T. canadensis* and the species' propensity to inhabit cove-like, cold air traps across the landscape (Cook and Cole, 1991). As the LWBI network across this region expands to include more *T. canadensis* chronologies as well as more high-elevation species, such as *P. rubens*, perhaps significant relationships between site latitude and/or elevation will be more clearly elucidated.

Further related to our analysis of site characteristics that might influence signal detection, we observed negative impacts of disturbance from hemlock woolly adelgid (HWA; *Adelges tsugae* Annand) at several sites across the MANE network. We experienced a failed attempt in May 2021 to update the Sweet Root Natural Area site in Pennsylvania, where we observed complete HWA-caused mortality of *T. canadensis* individuals that were originally cored at the site by Cook and Cole (1991) *ca.* 1982. The other site from which we observed marked impacts from HWA was Alander Mountain, Massachusetts. After coring this site in summer 2022 and developing the LWBI chronology, we noticed a severe impact in ring widths starting during the period 2006−2008 that was characterized by [1] narrow total and latewood widths that were also [2] light in color (*e.g.* thin tracheid walls throughout). Growth rings with such characteristics can bias BI data because of the absence of lignin caused by the disturbance agent, which in turn can weaken the climate signal fidelity. Given this narrow ring bias is most likely attributed

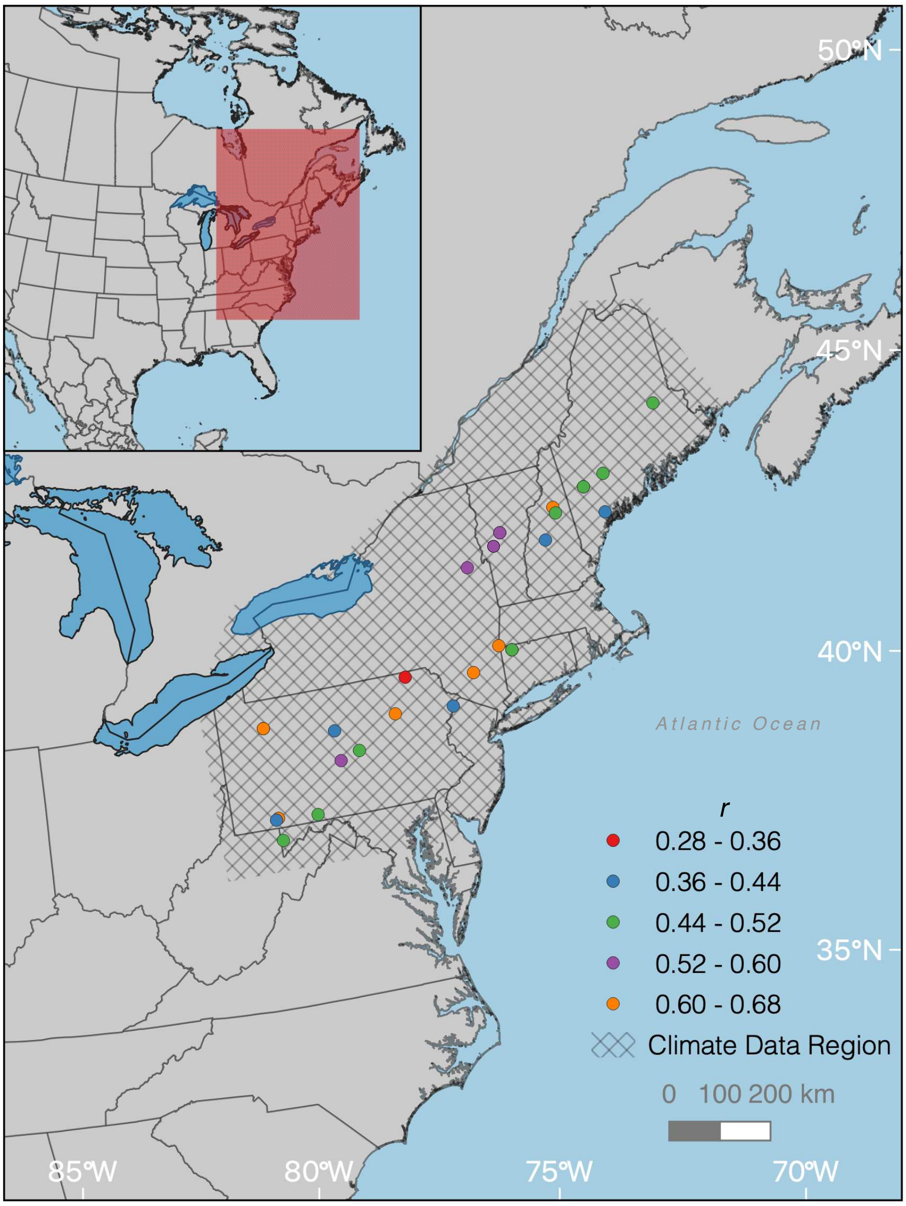


**Fig. 1 MANE BI network.** Map showing predictor chronology locations (dots) and target instrumental data (hatch) gathered from the CRU TS4.07 0.5°$T_{\text{Mar-Sep}}$ field (Harris et al., 2020) during the period 1901−1976. Colors indicate Pearson correlations ($p$<0.05) with the target instrumental data (hatch).

to the negative impacts of HWA at the site, we truncated this record to the year 2005, before which HWA impacted trees.

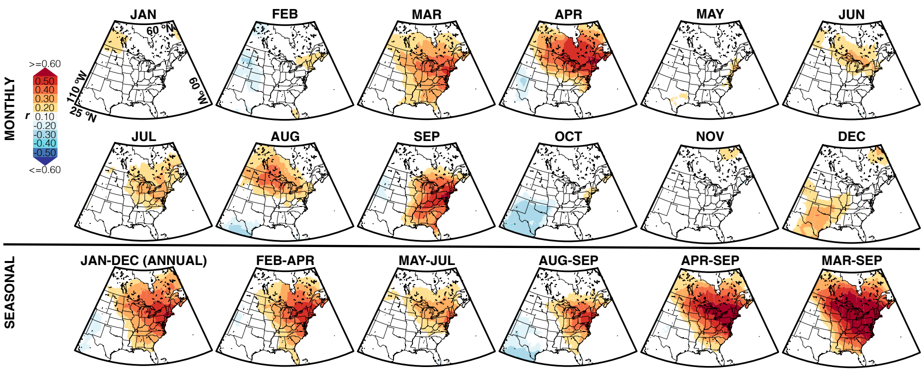


**Fig. 2 Temperature signal seasonality of the MANE LWBI network.** Monthly (top) and seasonal (bottom) correlations (Pearson's $r$; $p<0.05$) between $PC_1$ of the MANE BI network and $T_{\text{Mar-Sep}}$ (Harris et al., 2020) during the period 1901−1976.

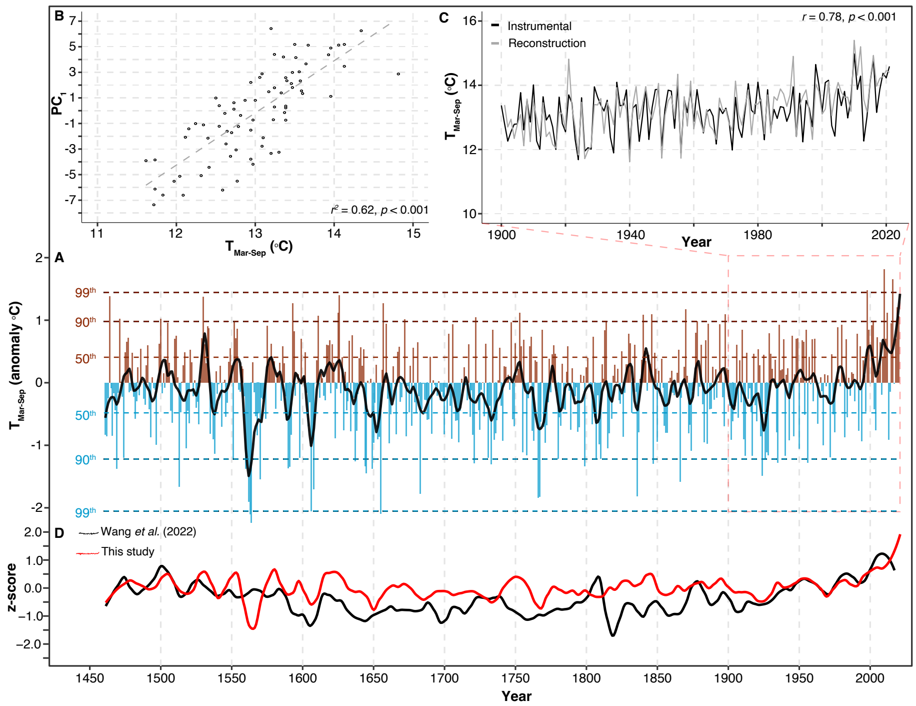


**Fig. 3 Reconstructed $T_{\text{Mar-Sep}}$ for MANE since 1461 CE.** (A) $T_{\text{Mar-Sep}}$ reconstruction shown as anomalies from 1461−2021 CE (red and blue bars) smoothed with a 20 y low pass filter (black) and 50,90, and 99$^{\text{th}}$ percentiles (dashed lines). (B) Scatter plot $T_{\text{Mar-Sep}}$ °C values versus $PC_1$ of the MANE BI network during the period 1901−1976. (C) Line graph showing agreement of the reconstruction (gray) and $T_{\text{Mar-Sep}}$ (black) during the period 1901−2021. (D) 50-year smoothed MANE temperature reconstruction (red) plotted together with a maximum latewood density (MXD)-based May-Aug reconstruction by Wang et al. (2022) (black) from eastern Canada. Pearson's correlation between the records is $r$ = 0.40 ($p<0.001$) during the period 1461−2017.

### 3.2 Model calibration and verification

The common period model spanned the period 1901−1976 over which the first PC (distilled from 29 sites and 983 tree cores) explains 62% of $T_{\text{Mar-Sep}}$ variance (Table S2; Figure 3B). The reconstruction comprised 16 backward nests extending to the year 1461. We also performed eight forward nests from 1977 to 2021. Going backward in time, the model nests remained robust, explaining over 40% of the instrumental variance with strong and positive RE (0.28-0.67) and CE (0.26-0.68) values until *ca.* 1550. The reconstruction remains valid with positive RE and CE statistics back to 1461 (Figure S3), however, as the number of tree-ring chronologies drops to $n$=2 at 1549, the calibration and verification period $R^2$ values decline to 0.20 and 0.37, respectively, weakening model estimates. Although the two nests before 1550 passed validation tests, the models explained 20% and 18% of the instrumental variance, hence values before 1550 should be interpreted with caution. The ability to place the current warming trend in a long-term context was a primary objective of this study. The explanatory power of forward model nests remained high until 2020 (46%) as a result of the abundance of updated tree-ring chronologies included in this study. The final temperature reconstruction benefited from these recollections and updates to *T. canadensis* chronologies that were originally sampled throughout the region in the late 1970s and through the 1980s and presented in Cook and Cole (1991).

### 3.3 MANE summer temperatures since 1461 CE

We provide a 561-year (1461−2021 CE) reconstruction of warm season $T_{\text{Mar-Sep}}$ for MANE (Figure 3A). The warmest reconstructed year is 2010 at +1.8 °C above the 1951−1980 mean, exceeding the 99$^{\text{th}}$ percentile. This finding is corroborated by the instrumental data, with 2010 having the warmest single-year summer since 1901 (+2.27 °C). The small discrepancy in anomalies calculated for the reconstruction versus the instrumental data highlights the fact that our reconstruction should be considered a conservative estimate of temperature due to general, yet slight, model underprediction (*e.g.* reconstructed warm (cool) years were most likely warmer (cooler) than estimated) (Esper et al., 2005) (Figure S1A-D). Assessment of model fit reveals an underestimation of target high-frequency variance particularly over the most recent *ca.* 20 years (Figures 3C; S4). This was expected given the reduction in predictor chronologies in the most recent forward nests. Given the propensity of MANE reconstruction model over- and under-predictions, bias-correction (Robeson et al., 2020) provided more accurate estimations of temperature for the reconstruction model (Figure S1B,D), and subsequently for the full reconstruction (Figure S1A).

Placing recent conditions within the context of the past 561 years, summer temperatures in 12 of the top 20 warmest single-year anomalies have occurred since the turn of the 21$^{\text{st}}$ century (2002, 2005, 2010−2012, 2015−2021) (Figure 4). The warmest multi-year events since 1461 were 2009−2012 ($\overline{x}$ anomaly +1.10 °C) and 2015−2021 ($\overline{x}$ +1.09 °C). Similar to the 21$^{\text{st}}$ century, the 16$^{\text{th}}$ century and early 17$^{\text{th}}$ centuries contain three of the most severe warm events, with 1593−1594 (+1.13 °C) being a short but intense positive departure, and 1575−1580 (+0.58 °C) and 1528−1534 (+ 0.78 °C) expressed as less intense but more prolonged

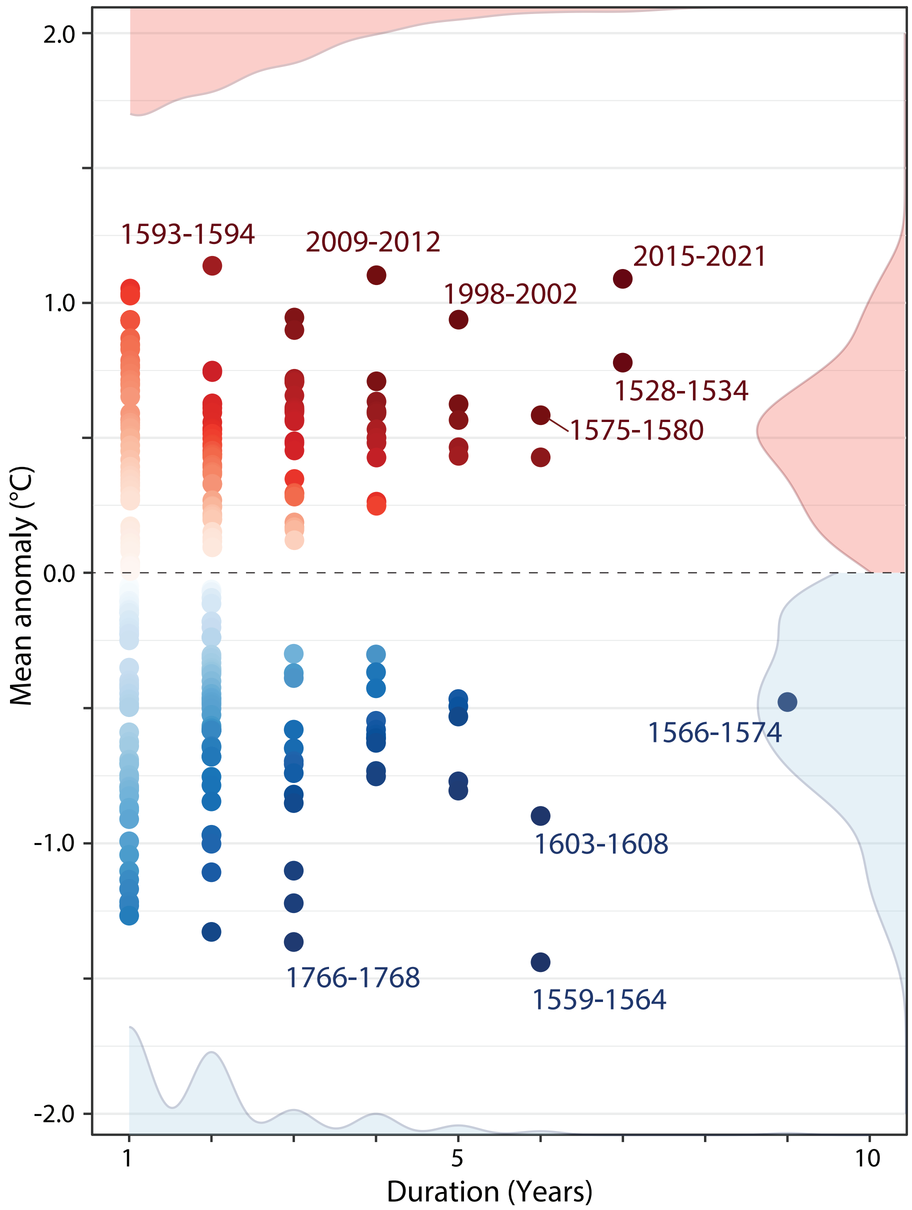


**Fig. 4 Severity-duration plot of the MANE $T_{Mar\text{-}Sep}$ reconstruction.** Bivariate characterization of multi-year warm (red) and cool (blue) events colored by magnitude (intensity/duration). Intensity (y-axis) and duration (x-axis) density plots shown on each margin.

departures. Unlike the 21$^{st}$ century, the 16$^{th}$−early 17$^{th}$ century also includes three of the most pronounced cool summer events across the region (-0.45 °C from 1566−1574, -0.87 °C from 1603−1608, and -1.4 °C from 1559−1564).

Our LWBI-based $T_{Mar\text{-}Sep}$ reconstruction shows multi-decadal agreement with previous studies that provided tree-ring-based temperature reconstructions for the region. Pearl et al. (2017) used *C. thyoides* growth rings to reconstruct mean Jan-Aug temperatures from 1872−2014. Although the pre-instrumental period of overlap between the two records is short, both records demonstrate a cooler-than-average 1870s followed by average temperature conditions before the cooling of the turn of the 20th century. Further, we find significant and positive multi-decadal coherence ($r$=0.40, $p$<0.001) with a maximum latewood density (MXD)-based reconstruction of mean May-Aug temperatures from northeastern North America (NENA) from 1461−2017—the common period of overlap between the two records (Wang et al., 2022) (Figure 3D). Although the length of our record precludes us from characterizing the historical context of modern warming as compared to the Medieval Climate Anomaly (MCA; *ca.* 950−1250 CE), we do capture the cooler-than-average summers of the Little Ice Age (LIA) during the 16th through 19th centuries. Most notable during this period are the aforementioned cool events of the late 16th−early 17th century, as well as the *ca.* 100-year period of cooler-than-average summers from 1640s−1740s, which is marked by reduced variability in the record. This period of cool summers is contemporary with the 16th century Megadrought that, although less severe in the eastern US compared to the western US, is still discernible in the North American Drought Atlas (Cook et al., 1999). One noteworthy distinction between the MANE and NENA reconstructions during the LIA is comparatively lower average summer temperatures expressed by NENA. We attribute this difference to [1] the higher-latitude and inland locations of predictor sites in Wang et al. (2022) compared to this study, and [2] the varied proxy indicators between the two studies; NENA is a record derived from MXD and we exclusively use BI.

One of the primary contributors to anomalously cool summer conditions is volcanic forcing (Esper et al., 2013, 2017; Büntgen et al., 2020). The influence of large-scale volcanic eruptions on summer temperatures is also apparent across eastern Canada (Gennaretti et al., 2014; Wang et al., 2022) as well as over adjacent lower latitudes. Across the MANE region the largest, global eruptions since the 15th century are responsible for average departures in temperature of -0.70 °C during the eruption year and -0.60 °C in the following year ($n$=12, $p$<0.05, Figure S5). The most severe summer cooling event in the Wang et al. (2022) NENA reconstruction occurred in 1816 in response to the eruption of Mount Tambora in April 1815, marked as a -4.53 °C departure from the 1905−2006 CE mean. Pearl et al. (2020b) built upon their earlier study and produced a gridded field reconstruction of Jan-Aug temperatures since the early 1800s for the Northeast US. In response to the eruption of Tambora, they highlight widespread cooling of 1−3 °C across much of the region that lasted for two years (1816−1817) as one of the coldest periods in the reconstruction. We note a response to summer temperatures across MANE to the 1815 eruption with a departure from mean conditions starting in 1815 (-1.05 °C) and persisting until 1818, with an average temperature anomaly of -0.68 °C during this time. Although we observe a slight cooling event in response to the Tambora eruption, our reconstruction suggests that summer temperature departures were not as extreme across MANE compared to the higher latitude Wang et al. (2022) study. Yet, differences in seasonality (e.g. Mar-May for NENA versus Mar-Sep for MANE) and the ability of various proxies to precisely capture the imprint of volcanic cooling (*e.g.* MXD versus BI; (Edwards et al., 2021)) might explain this disparity. Perhaps a more intriguing difference between the NENA and MANE summer temperature records is the timing of volcanic forcing on temperature departures. The NENA reconstruction (772−2017 CE) demonstrates a consistent one-year lag, particularly in response to volcanic eruptions from tropical locations. While we also note a significant ($p<0.05$) one-year lag response of MANE temperatures to eruptions, the 0-lag year (year of) eruption resulted in cooler temperature departures. This discrepancy in timing—potentially due to latitudinal, seasonality, and parameter input differences—presents an opportunity to disentangle the effects of eruption origin (tropical vs extra-tropical) and timing on summer cooling, especially as temperature-sensitive tree-ring records continue to develop across the Northern Hemisphere (Kaczka and Wilson, 2021). Yet, developing QWA metrics for each record will be necessary to quantify differences in the timing response to volcanic forcing (Edwards et al., 2021).

### 3.4 Ocean/atmosphere drivers of MANE temperatures

In addition to the influence of past volcanic eruptions, we find a strong association between the latitudinal position of the NHJ and MANE $T_{\text{Mar-Sep}}$ (Figure 5). Belmecheri et al. (2017)—who provide analyses of the relationships between seasonal 300-hpa NHJ positions and precipitation and temperature since 1930 CE across North America—note that the position of the NHJ during summer displays a dipole pattern characterized by positive temperature anomalies across the MANE region associated with higher latitude NHJ trajectories. Using predictor chronologies completely independent of those used for MANE, Trouet et al. (2018) build on this study and reconstruct the latitudinal position of the August NHJ since 1725 (Figure 5A). We find that years during which the latitudinal position of the Aug NHJ was $>55\ ^{\circ}$N produced warmer summers (Figure 5B). Conversely, when the NHJ migrates to a dominant lower-latitude position ($<48\ ^{\circ}$N), summer conditions are cooler (Figure 5C). In support of this connection, we find that increased 300-hpa meridional (zonal) wind stress produces decreased (increased) summer temperatures across MANE (Figure 6A,B). The negative correlation ($r$ range -0.20 to -0.50, $p<0.05$) between meridional wind stress and summer temperatures over MANE matches the "JA-6" (JA=July-August or summer season; (Belmecheri et al., 2017)) longitudinal position pattern of the NHJ, whereby a meridional undulation funnels high-latitude air towards the lower latitude MANE region. Conversely, increased zonal wind stress north of $\sim55\ ^{\circ}$N, as shown in Figure 6B, results in warmer summer temperatures, most likely due to the facilitation of higher pressure over the region as well as over the British Isles (Figure 6C), a pattern also highlighted by Belmecheri et al. (2017). This association is also supported by the spatial footprint of the Trouet et al. (2018) NHJ reconstruction model, which shows strong relationships between the Aug NHJ position and instrumental air temperatures over central North America during the period 1920−2012. NHJ positions that are 1 SD northwards (southwards) from the mean position display higher (lower) August temperature anomalies. However, we do note that the relationships between latitudinal NHJ position and temperature anomalies seem to be strongest over central North America, centered over the Great Lakes region as described in Figure 1A,B from Trouet et al. (2018). Despite not including any sites outside the MANE area, our reconstruction demonstrates strong spatial correlations over the Great Lakes, broader Upper Midwest US, and central Canada ($r \geq 0.60$, $p<0.001$; Figure S6). Thus, we highlight the need to develop temperature-sensitive proxies (*e.g.* LWBI, MXD, QWA) over the Great Lakes region to combine with existing records across MANE and the Pacific Northwest (Heeter et al., 2023) to increase our understanding of continental-scale linkages between NHJ dynamics and summer temperature anomalies (Trouet et al., 2018).

Our analysis shows a significant ($r>0.50$, $p<0.05$) spatial relationship between the MANE reconstruction and sea surface temperatures (SST) in the adjacent, near-shore Atlantic Ocean centered around the Gulf of Maine (Figure 6D). Pearl et al. (2017) and Pearl et al. (2020b) demonstrated the same significant and positive relationship between Northeast US land and SSTs, although they report a broader spatial connection over much of the North Atlantic Ocean. Most MANE predictors are positioned considerably inland and at higher elevations compared to the coastal *C. thyoides* chronologies included in previous Northeast US temperature reconstructions (Pearl et al., 2017, 2020b), most likely explaining the differences in spatial imprint of SSTs. A multi-proxy network that combines the strong temperature proxies of *C. thyoides* (Pearl et al., 2020b) with the LWBI-derived MANE network as well as other tree-ring width chronologies from the region shown to demonstrate a sensitivity to growing season temperatures (Patterson et al., 2016) would produce a potentially more robust pool of candidate predictors across a region known for diverse and complex relationships between tree species and temperature Pederson et al. (2004); Alexander et al. (2019); Maxwell et al. (2020).

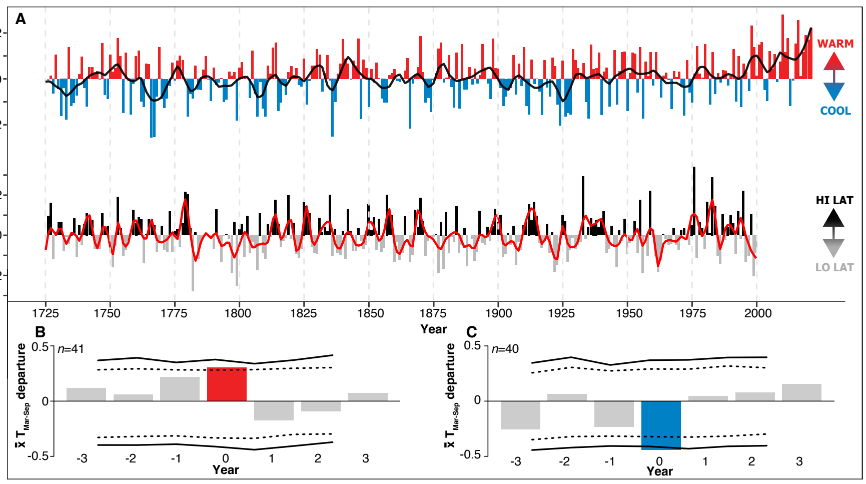


**Fig. 5 Association between the latitudinal position of the Northern Hemisphere polar jet stream (NHJ) and reconstructed MANE $T_{Mar\text{-}Sep}$ since 1725 CE.** (A) 31-year smoothed (LOESS) anomaly time series of the $T_{Mar\text{-}Sep}$ reconstruction and reconstructed NHJ from Trouet et al. (2018). (B) and (C) show superposed epoch analysis results of significant ($p<0.05$=dotted;$p<0.01$=solid) departures in mean temperature (red=warm, blue=cool) during ±2 SD in NHJ latitudinal positions.

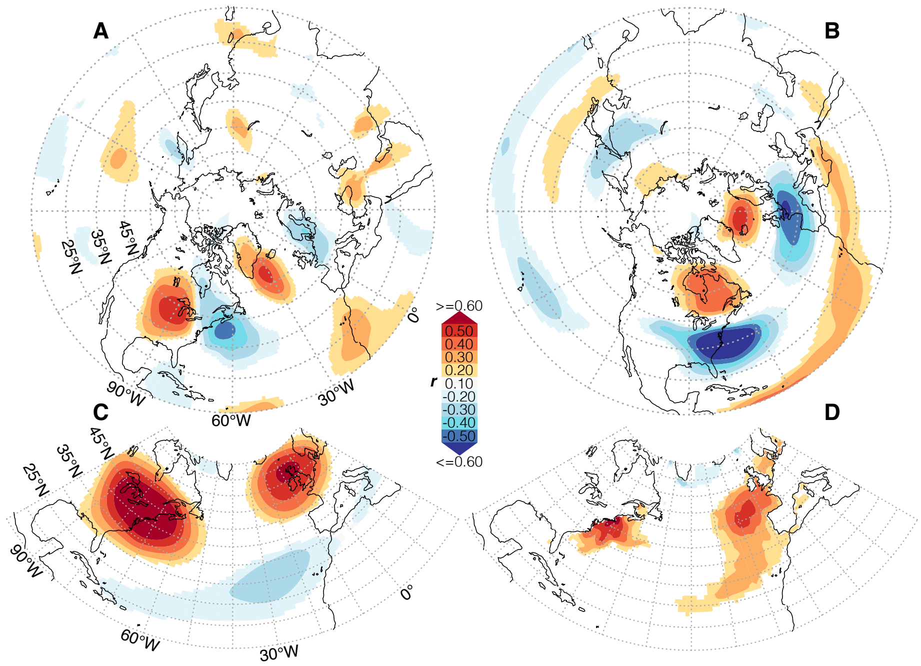


**Fig. 6 Dynamical climate characteristics of the MANE $T_{Mar\text{-}Sep}$ reconstruction.** Spatial correlation (1*st*-differenced) between the MANE $T_{Mar\text{-}Sep}$ reconstruction versus 300-hpa meridional (A) and zonal (B) wind stress (20CRv3) during the period 1901−2021, (C) 500-hpa geopotential height (20CRv3; 1901−2021), and (D) sea surface temperatures (HadISST) 1901−2021.

## 4 Conclusions

Assessment of an improved network of BI tree-ring chronologies across the MANE region reveals an unprecedented warming trend over the past 30 years including 12 of the top 20 warmest summers since 1461 CE. Temperature variability across MANE is linked with latitudinal and longitudinal undulations of the NHJ and large-scale volcanic eruptions. The expansion of the LWBI-derived MANE network to the west and south and the combination with existing temperature-sensitive proxies across North America (Heeter et al., 2020, 2021; Wilson et al., 2019; Wiles et al., 2019; Edwards et al., 2021; Trinies et al., 2022; Gennaretti et al., 2014; Wang et al., 2022; Heeter et al., 2019) will be critical for a more comprehensive understanding of spatiotemporal dynamics of temperature variability over the last millennium (*e.g.* values, trends, compound climate extremes). This would foster our insights into the direct impact of a more volatile NHJ on summer temperatures and support the disentanglement of the spatial imprint and timing of past volcanic eruptions on temperature departures. Such improvements to the MANE network, however, are challenging as many viable species for BI in the eastern US (Harley et al., 2021) are already included in the MANE network. This could be overcome by developing BI chronologies from *P. rubens* that would offer additional sites across the species range and at higher elevations, which might lead to more comprehensive estimations of temperatures. Moreover, the temporal extension of BI chronologies can be achieved by successfully including subfossil and historical material retrieved across the Mid-Atlantic and Northeast USA, which dates as far back as at least the past several thousand years (Pearl et al., 2020a). We, therefore, propose to extend the MANE network back in time through [1] the application of QWA or BI to existing subfossil *C. thyoides* material (Pearl et al., 2020a) using resin-extraction processes outlined in Heeter et al. (2022) and [2] the acquisition of old-growth *T. canadensis* and *P. rubens* used in historical structures or found at the bottom of cold lakes (Lorentzen, 2023; Krusic et al., 2015).

## 5 Acknowledgments

This research is funded by the US National Science Foundation Paleo Perspectives on Climate Change program (P2C2; AGS-1805276, AGS-1805617, AGS-2002524, AGS-2002482) and the Geographical Sciences Program (BCS-1229887). F.R. and J.E. were funded by the ERC Advances project Monostar (AdG 882727). We wish to thank the personnel at the following locations for granting access: Great Mountain Forest, Howland, Maine Division of Parks and Public Lands, Mattawamkeag Wilderness Park, New Hampshire Division of Forests and Lands, The Nature Conservancy, University of Maine, Vermont Department of Parks and Recreation, White Mountain National Forest, Paradise Point Audubon Center, New York Department of Environmental Conservation, New York Parks, Recreation and Historic Preservation and Minnewaska State Park Preserve, USFS Research Natural Areas, and the US Forest Service. We also thank the following people for assisting with the fieldwork components of this research: Fosca Bechthold, Dina Cordes, April Kaiser, Benjamin Lockwood, Trevis Matheus, Neil Pederson, Karly Schmidt, Philipp Schultz, and Matthew Wenzel.

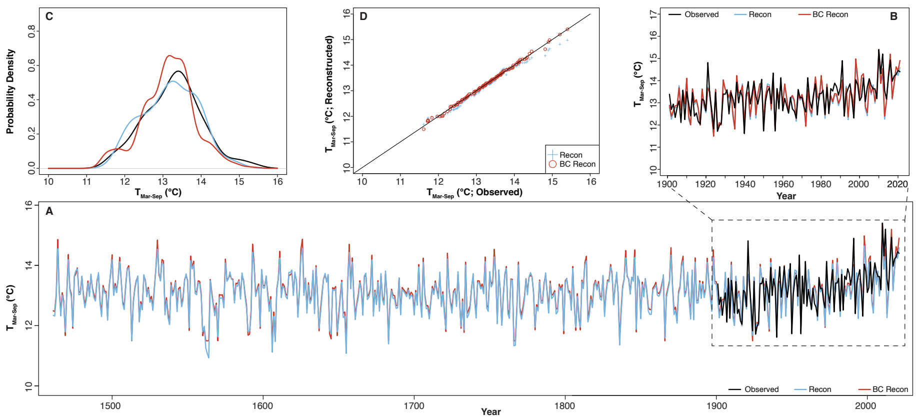


**Fig. S1 MANE $T_{Mar\text{-}Sep}$ reconstruction bias correction.** (A) Time series of uncorrected (blue) and bias-corrected (BC; red) $T_{Mar\text{-}Sep}$ reconstruction spanning 1461−2021 CE plotted with instrumental Mar-Sep CRU TS4.07 $T_{Mar\text{-}Sep}$ data during the period 1901−2021 (black) [zoom inset shown as (B)]. (C) Probability density functions for the uncorrected (blue) and bias-corrected and instrumental data (black). (D) Quantitle-quantile plot of the uncorrected (blue) and bias-corrected (red) reconstructions.

**Table S1** Chronology site information used in the MANE $T_{\text{Mar-Sep}}$ reconstruction. Site statistics and location correspond with Figure 1. All collections are *T. canadensis* except for Cape Natural Research Area (*P. rubens*). $r$ = correlation coefficient versus target instrumental data, $\beta$ = beta weight, ITRDB DOI=hyperlink to International Tree Ring Data Bank data

| Site Name | $r$ | $\beta$ | Lat (N°) | Long. (W°) | Start | End | ITRDB DOI |
|---|---|---|---|---|---|---|---|
| Alan Seeger Natural Area | 0.59 | 0.09 | 40.70 | -77.75 | 1609 | 2013 | — |
| Alander Mountain | 0.68 | 0.12 | 42.09 | -73.51 | 1779 | 2005 | — |
| Bear Run Nature Preserve | 0.65 | 0.11 | 39.90 | -79.44 | 1646 | 2020 | — |
| Bigelow Pond | 0.46 | 0.06 | 41.96 | -73.22 | 1655 | 1986 | CT001 |
| Bigelow Pond Recollect | 0.44 | 0.05 | 41.96 | -73.22 | 1646 | 2012 | CT004 |
| Boody Pond | 0.44 | 0.05 | 44.57 | -69.98 | 1747 | 2012 | ME042 |
| Boody Pond Update | 0.56 | 0.09 | 44.57 | -69.98 | 1768 | 2022 | — |
| Bradbury Mountain State Park | 0.41 | 0.05 | 43.90 | -70.18 | 1896 | 2012 | ME043 |
| Cape Research Natural Area | 0.52 | 0.06 | 43.81 | -72.98 | 1811 | 2009 | — |
| Dingmans Falls | 0.44 | 0.05 | 41.23 | -74.89 | 1607 | 2020 | — |
| East Branch Swamp Natural Area | 0.37 | 0.04 | 41.23 | -77.77 | 1511 | 1981 | PA004 |
| Ferncliff Peninsula Natural Area | 0.43 | 0.05 | 39.87 | -79.50 | 1623 | 2020 | — |
| Gibbs Brook | 0.63 | 0.11 | 44.22 | -71.40 | 1660 | 2013 | NH002 |
| Granville Gulf State Forest | 0.38 | 0.04 | 44.02 | -72.83 | 1633 | 1981 | VT002 |
| Granville Gulf State Forest Update | 0.57 | 0.09 | 44.02 | -72.83 | 1785 | 2020 | — |
| Little Concord Pond | 0.45 | 0.07 | 44.43 | -70.53 | 1681 | 2012 | ME045 |
| Little Concord Pond Update | 0.47 | 0.07 | 44.43 | -70.53 | 1761 | 2022 | — |
| Mattawamkeag Wilderness Park | 0.45 | 0.05 | 45.52 | -68.28 | 1677 | 2012 | ME046 |
| Nancy Brook | 0.48 | 0.07 | 44.12 | -71.37 | 1627 | 2021 | — |
| Pack Forest | 0.57 | 0.09 | 43.56 | -73.81 | 1542 | 2021 | — |
| Paradise Point Trail | 0.42 | 0.05 | 43.70 | -71.78 | 1643 | 2021 | — |
| Ricketts Glen State Park | 0.63 | 0.10 | 41.31 | -76.28 | 1621 | 2020 | — |
| Salt Springs State Park | 0.28 | 0.02 | 41.91 | -75.87 | 1620 | 1981 | PA011 |
| Snyder Middleswarth Natural Area | 0.51 | 0.08 | 40.81 | -77.29 | 1762 | 2020 | — |
| Spruce Glen | 0.64 | 0.11 | 41.73 | -74.24 | 1654 | 2021 | — |
| Swallow Falls State Park | 0.49 | 0.06 | 39.50 | -79.42 | 1694 | 2020 | — |
| Sweetroot Natural Area | 0.45 | 0.05 | 39.84 | -78.52 | 1612 | 1981 | PA012 |
| Tionesta | 0.49 | 0.05 | 41.50 | -79.43 | 1461 | 1978 | PA013 |
| Tionesta Update | 0.62 | 0.11 | 41.50 | -79.43 | 1603 | 2021 | — |

**Table S2** Nested reconstruction model statistics. Northeast US $T_{Mar\text{-}Sep}$ nested reconstruction model statistics, including the common period model (CP) with backward (B) and forward (F) model nests for the period 1461-2021 CE. # CRNS=number of tree-ring chronologies, # CORES=number of individual tree cores, $CR^2/VR^2$=calibration/verification period coefficient of determination, VRE/VCE=verification period reduction of error/coefficient of efficiency, RMSE=root mean-squared error

| Nest | Period | # CRNS | # CORES | $CR^2$ | $VR^2$ | VRE | VCE | RMSE |
|---|---|---|---|---|---|---|---|---|
| F8 | 2020-2021 | 2 | 55 | 0.18 | 0.10 | 0.11 | 0.06 | 0.68 |
| F7 | 2014-2020 | 8 | 227 | 0.46 | 0.38 | 0.41 | 0.38 | 0.55 |
| F6 | 2012-2013 | 15 | 406 | 0.50 | 0.45 | 0.46 | 0.38 | 0.52 |
| F5 | 2006-2012 | 16 | 426 | 0.56 | 0.45 | 0.47 | 0.44 | 0.51 |
| F4 | 1987-2005 | 17 | 466 | 0.57 | 0.52 | 0.54 | 0.52 | 0.48 |
| F3 | 1982-1986 | 23 | 597 | 0.53 | 0.52 | 0.53 | 0.51 | 0.46 |
| F2 | 1979-1981 | 24 | 812 | 0.61 | 0.65 | 0.65 | 0.64 | 0.41 |
| F1 | 1977-1978 | 28 | 947 | 0.62 | 0.66 | 0.67 | 0.66 | 0.41 |
| CP | 1896-1976 | 29 | 983 | 0.62 | 0.67 | 0.67 | 0.66 | 0.41 |
| B1 | 1790-1895 | 28 | 801 | 0.62 | 0.67 | 0.67 | 0.66 | 0.41 |
| B2 | 1780-1789 | 27 | 415 | 0.62 | 0.68 | 0.67 | 0.66 | 0.41 |
| B3 | 1770-1779 | 26 | 395 | 0.61 | 0.67 | 0.67 | 0.66 | 0.42 |
| B4 | 1750-1769 | 23 | 360 | 0.62 | 0.70 | 0.69 | 0.68 | 0.41 |
| B5 | 1700-1749 | 22 | 300 | 0.62 | 0.69 | 0.69 | 0.68 | 0.41 |
| B6 | 1690-1699 | 21 | 168 | 0.62 | 0.68 | 0.68 | 0.67 | 0.41 |
| B7 | 1680-1689 | 19 | 144 | 0.63 | 0.68 | 0.68 | 0.67 | 0.41 |
| B8 | 1660-1679 | 18 | 116 | 0.63 | 0.67 | 0.67 | 0.67 | 0.41 |
| B9 | 1650-1659 | 15 | 77 | 0.59 | 0.63 | 0.63 | 0.62 | 0.43 |
| B10 | 1640-1649 | 12 | 61 | 0.58 | 0.62 | 0.63 | 0.62 | 0.44 |
| B11 | 1630-1639 | 11 | 52 | 0.53 | 0.63 | 0.63 | 0.62 | 0.43 |
| B12 | 1620-1629 | 8 | 46 | 0.56 | 0.61 | 0.61 | 0.60 | 0.44 |
| B13 | 1610-1619 | 6 | 39 | 0.55 | 0.63 | 0.63 | 0.62 | 0.45 |
| B14 | 1550-1609 | 3 | 28 | 0.41 | 0.47 | 0.47 | 0.45 | 0.51 |
| B15 | 1520-1549 | 2 | 9 | 0.20 | 0.37 | 0.32 | 0.30 | 0.60 |
| B16 | 1461-1519 | 1 | 5 | 0.18 | 0.36 | 0.28 | 0.26 | 0.60 |

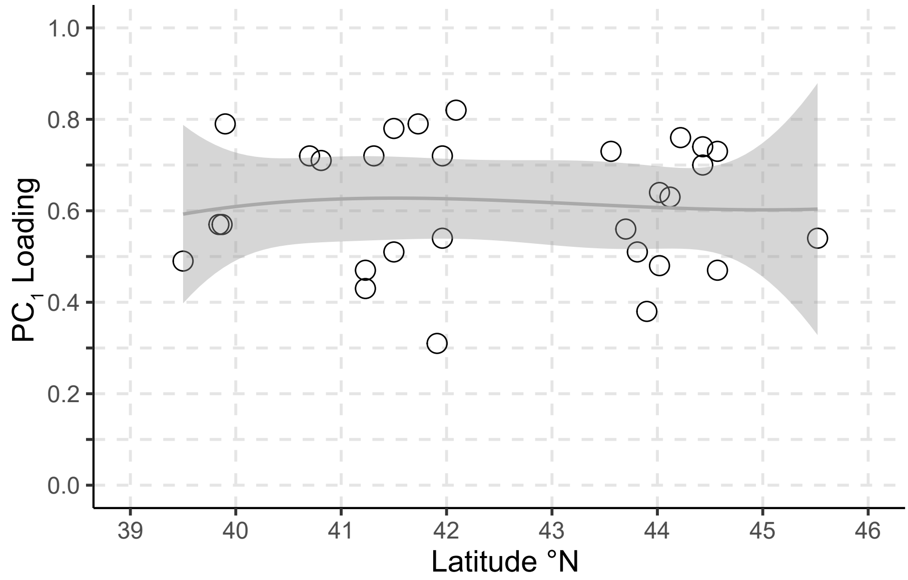


**Fig. S2 MANE LWBI network $PC_1$ loadings versus latitude.** $PC_1$ loadings of the 29 predictor sites plotted against site latitude. Solid gray line is a 2$^{nd}$-order polynomial function with 2-$\sigma$ error (gray envelop) to show non-linear relationship between latitude and loadings.

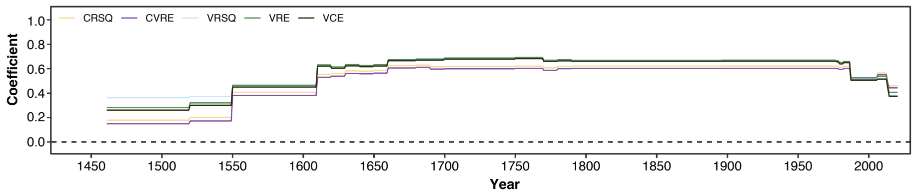


**Fig. S3 MANE $T_{Mar\text{-}Sep}$ reconstruction validation statistics.** Reconstruction validation statistics for each nest showing calibration period R2 (yellow), verification period R2 (purple), verification period reduction of error (green), and verification period coefficient of efficiency (blue).

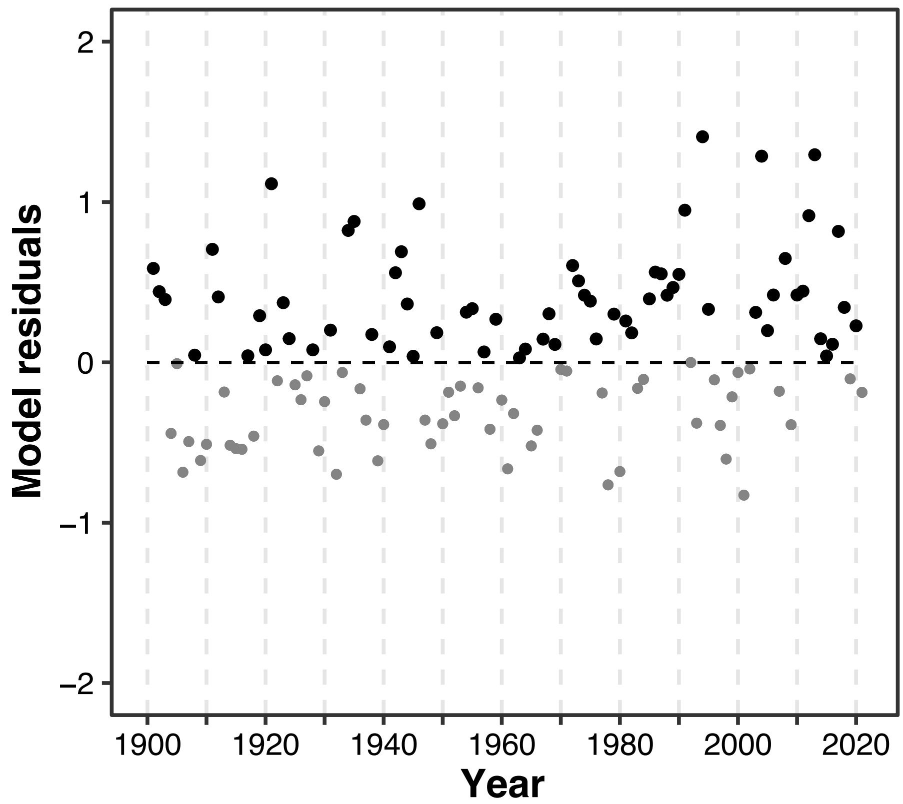


**Fig. S4 MANE $T_{Mar\text{-}Sep}$ reconstruction model residuals.** Predicted values subtracted from actual values (CRU TS4.07; (Harris et al., 2020)) during the period 1901-2021. Positive (black dot) values are underpredictions and negative (gray dot) values are overpredictions.

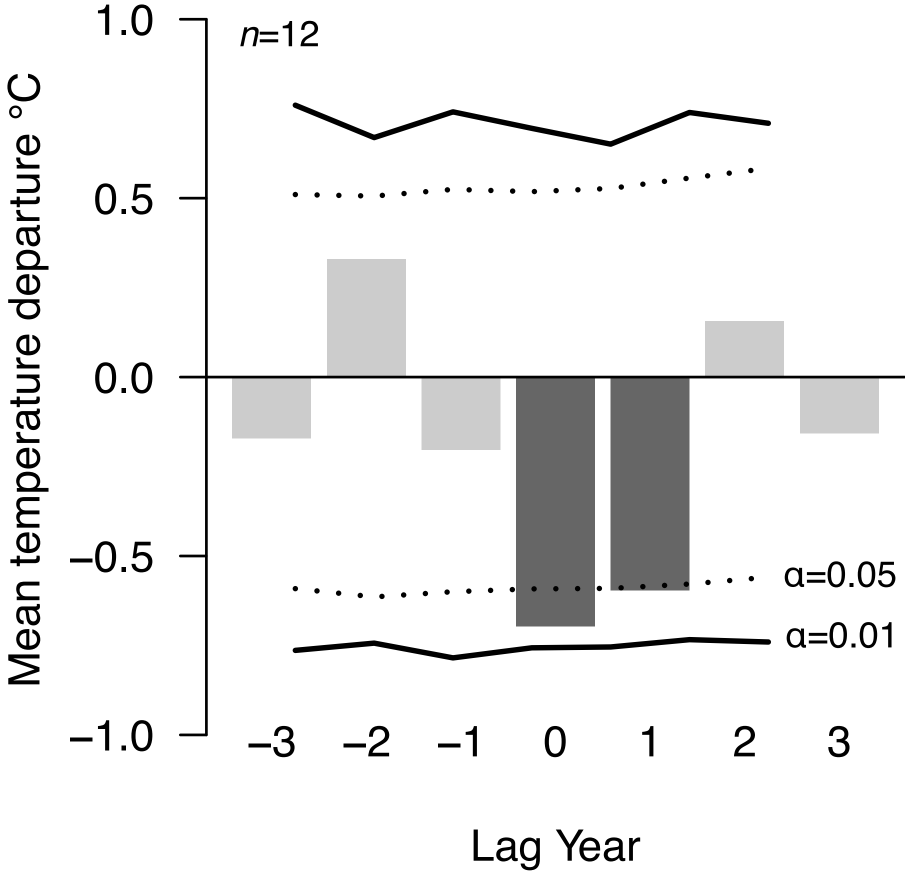


**Fig. S5 Global volcanic eruption impacts on MANE summer temperatures.** Superposed epoch analysis between the reconstruction time series and the largest volcanic eruptions from 1461-1900 CE based on estimated aerosol optical depth (Toohey and Sigl, 2017) with additional large, instrumental-period eruptions of 1912 (Novarupta), Agung (1963), 1982 (El Chicon), and 1991 (Pinatubo) included.

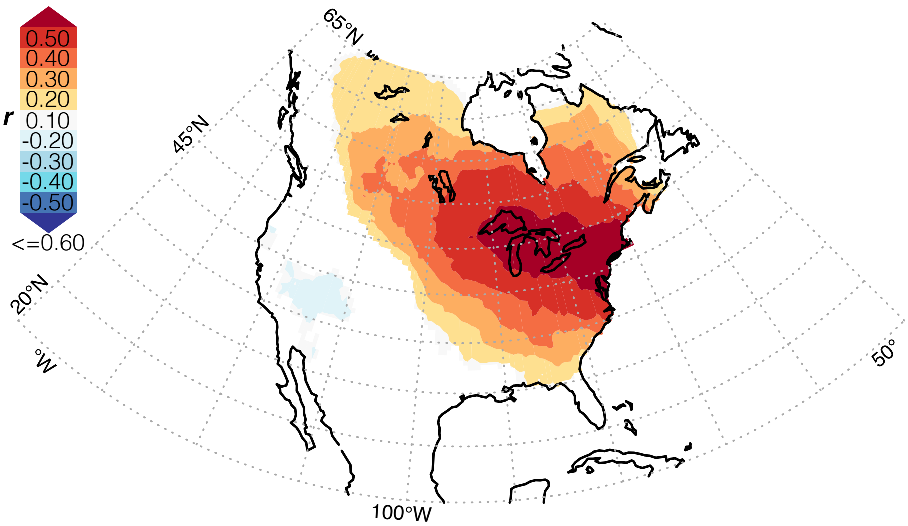


**Fig. S6 Spatial footprint of the MANE $T_{Mar\text{-}Sep}$ reconstruction.** Map showing the spatial Pearson's correlation ($p$<0.01) between $PC_1$ of the LWBI records included in the MANE network and gridded CRU TS4.07 $T_{Mar\text{-}Sep}$ during the period 1901−1976. Site information for each location is available in Table S1.

## References


Akaike H (1974) A new look at the statistical model identification. In: Selected Papers of Hirotugu Akaike, Springer, pp 215–222

Alexander MR, Pearl JK, Bishop DA, Cook ER, Anchukaitis KJ, Pederson N (2019) The potential to strengthen temperature reconstructions in ecoregions with limited tree line using a multispecies approach. Quaternary Research 92(2):583–597

Anchukaitis KJ, Wilson R, Briffa KR, Büntgen U, Cook ER, D'Arrigo R, Davi N, Esper J, Frank D, Gunnarson BE, et al. (2017) Last millennium northern hemisphere summer temperatures from tree rings: Part ii, spatially resolved reconstructions. Quaternary Science Reviews 163:1–22

Belmecheri S, Babst F, Hudson AR, Betancourt J, Trouet V (2017) Northern hemisphere jet stream position indices as diagnostic tools for climate and ecosystem dynamics. Earth Interactions 21(8):1–23

Belmecheri S, Maxwell RS, Taylor AH, Davis KJ, Guerrieri R, Moore DJ, Rayback SA (2021) Precipitation alters the co2 effect on water-use efficiency of temperate forests. Global Change Biology 27(8):1560–1571

Bunn AG (2008) A dendrochronology program library in r (dplr). Dendrochronologia 26(2):115–124

Bunn AG (2010) Statistical and visual crossdating in r using the dplr library. Dendrochronologia 28(4):251–258

Büntgen U, Arseneault D, Boucher É, Churakova OV, Gennaretti F, Crivellaro A, Hughes MK, Kirdyanov AV, Klippel L, Krusic PJ, et al. (2020) Prominent role of volcanism in common era climate variability and human history. Dendrochronologia 64:125757

Cao X, Hu H, Kao Pk, Buckley BM, Dong Z, Chen X, Zhou F, Fang K (2022) Improved spring temperature reconstruction using earlywood blue intensity in southeastern china. International Journal of Climatology 42(12):6204–6220

Compo GP, Whitaker JS, Sardeshmukh PD, Matsui N, Allan RJ, Yin X, Gleason BE, Vose RS, Rutledge G, Bessemoulin P, et al. (2011) The twentieth century reanalysis project. Quarterly Journal of the Royal Meteorological Society 137(654):1–28

Conkey LE (1986) Red spruce tree-ring widths and densities in eastern North America as indicators of past climate. Quaternary Research 26(2):232–243

Cook ER, Cole J (1991) On predicting the response of forests in Eastern North America to future climatic change 19:271–282

Cook ER, Peters K (1981) The smoothing spline: a new approach to standardizing forest interior tree-ring width series for dendroclimatic studies. Tree-Ring Bulletin 41:45–53

Cook ER, Peters K (1997) Calculating unbiased tree-ring indices for the study of climatic and environmental change. The Holocene 7(3):361–370

Cook ER, Meko DM, Stahle DW, Cleaveland MK (1999) Drought reconstructions for the continental united states. Journal of Climate 12(4):1145–1162

Cook ER, Woodhouse CA, Eakin CM, Meko DM, Stahle DW (2004) Long-term aridity changes in the western united states. Science 306(5698):1015–1018

Cook ER, Seager R, Cane MA, Stahle DW (2007) North American drought: Reconstructions, causes, and consequences. Earth Science Reviews 81(1-2):93–134

Edwards J, Anchukaitis KJ, Zambri B, Andreu-Hayles L, Oelkers R, D'Arrigo R, von Arx G (2021) Intra-annual climate anomalies in northwestern north america following the 1783-1784 ce laki eruption. Journal of Geophysical Research: Atmospheres p e2020JD033544

Esper J, Cook ER, Schweingruber FH (2002) Low-frequency signals in long tree-ring chronologies for reconstructing past temperature variability. science 295(5563):2250–2253

Esper J, Frank DC, Wilson RJS, Briffa KR (2005) Effect of scaling and regression on reconstructed temperature amplitude for the past millennium. Geophys Res Lett 32(7), DOI 10.1029/2004gl021236

Esper J, Schneider L, Krusic PJ, Luterbacher J, Büntgen U, Timonen M, Sirocko F, Zorita E (2013) European summer temperature response to annually dated volcanic eruptions over the past nine centuries. Bulletin of volcanology 75:1–14

Esper J, Büntgen U, Hartl-Meier C, Oppenheimer C, Schneider L (2017) Northern hemisphere temperature anomalies during the 1450s period of ambiguous volcanic forcing. Bulletin of Volcanology 79:1–9

Foster JR, D'Amato AW (2015) Montane forest ecotones moved downslope in northeastern usa in spite of warming between 1984 and 2011. Global Change Biology 21(12):4497–4507

Francis JA, Vavrus SJ (2015) Evidence for a wavier jet stream in response to rapid arctic warming. Environmental Research Letters 10(1):014005

Francis JA, Chan W, Leathers DJ, Miller JR, Veron DE (2009) Winter northern hemisphere weather patterns remember summer arctic sea-ice extent. Geophysical Research Letters 36(7)

Frank D, Esper J, Cook ER (2007) Adjustment for proxy number and coherence in a large-scale temperature reconstruction. Geophysical Research Letters 34(16)

Fritts H (1976) Tree rings and climate. Elsevier

Gennaretti F, Arseneault D, Nicault A, Perreault L, Bégin Y (2014) Volcano-induced regime shifts in millennial tree-ring chronologies from northeastern north america. Proceedings of the National Academy of Sciences 111(28):10077–10082

González J, Valdés JB (2003) Bivariate drought recurrence analysis using tree ring reconstructions. Journal of Hydrologic Engineering 8(5):247–258

Guttman L (1954) Some necessary conditions for common-factor analysis. Psychometrika 19(2):149–161

Harley GL, Heeter KJ, Maxwell JT, Rayback SA, Maxwell RS, Reinemann TE, H Taylor A (2021) Towards broad-scale temperature reconstructions for eastern north america using blue light intensity from tree rings. International Journal of Climatology 41:E3142–E3159

Harris I, Osborn TJ, Jones P, Lister D (2020) Version 4 of the cru ts monthly high-resolution gridded multivariate climate dataset. Scientific data 7(1):109

Heeter KJ, Harley GL, Van De Gevel SL, White PB (2019) Blue intensity as a temperature proxy in the eastern united states: A pilot study from a southern disjunct population of picea rubens (sarg.). Dendrochronologia 55:105–109

Heeter KJ, Harley GL, Maxwell JT, McGee JH, Matheus TJ (2020) Late summer temperature variability for the Southern Rocky Mountains (USA) since 1735 CE: applying blue light intensity to low-latitude Picea engelmannii Parry ex Engelm. Climatic Change pp 1–24

Heeter KJ, Rochner ML, Harley GL (2021) Summer air temperature for the Greater Yellowstone Ecoregion (770–2019 CE) over 1,250 years. Geophysical Research Letters 48(7):e2020GL092269

Heeter KJ, King DJ, Harley GL, Kaczka RJ (2022) Video tutorial: Measuring blue intensity with the coorecorder software application. Dendrochronologia 76:125999

Heeter KJ, Harley GL, Abatzoglou JT, Anchukaitis KJ, Cook ER, Coulthard BL, Dye LA, Homfeld IK (2023) Unprecedented 21st century heat across the pacific northwest of north america. npj Climate and Atmospheric Science 6(1):5

Hopton HM, Pederson N (2005) Climate sensitivity of atlantic white cedar at its northern range limit. In: Atlantic White Cedar: Ecology, Restoration and Management: Proceedings of the Arlington Echo Symposium. Gen. Tech. Rep. SRS-91. USDA-Forest Service, Southern Research Station, Asheville, NC. Asheville, NC: USDA Forest Service Southern Research Station, pp 22–30

Horton R, Yohe G, Easterling W, Kates R, Ruth M, Sussman E, Whelchel A, Wolfe D, Lipschultz FC (2014) Northeast. climate change impacts in the united states: The third national climate assessment. US Global Change Research Program pp 16–1

Jones PD, Briffa KR, Barnett TP, Tett SFB (1998) High-resolution palaeoclimatic records for the last millennium: interpretation, integration and comparison with General Circulation Model control-run temperatures. Holocene 8:455–471

Kaczka RJ, Wilson R (2021) I-bind: International blue intensity network development working group. Dendrochronologia 68:125859

Kaiser HF (1960) The application of electronic computers to factor analysis. Educational and psychological measurement 20(1):141–151

Kosiba AM, Schaberg PG, Rayback SA, Hawley GJ (2018) The surprising recovery of red spruce growth shows links to decreased acid deposition and elevated temperature. Science of the Total Environment 637:1480–1491

Krusic P, Flynt B, Macadeag G, Ladolcetta M, Benjamin J (2015) 25th Annual North American Dendroecological Fieldweek Final Report. Tech. Rep. https://sites.google.com/view/nadef/past-fieldweeks/2015, NADEF, Acadia National Park, Maine

Kunkel KE, Stevens LE, Stevens SE, Sun L, Janssen E, Wuebbles D, Hilberg SD, Timlin MS, Stoecker L, Westcott N, et al. (2013) Regional climate trends and scenarios for the us national climate assessment part 3. climate of the midwest us. NOAA Technical Report NESDIS 142-3

Larsson L (2014) Coorecorder and cdendro programs of the coorecorder/cdendro package version 7.7

Lorentzen B (2023) personal communication.

Mann ME, Bradley RS, Hughes MK (1999) Northern hemisphere temperatures during the past millennium: Inferences, uncertainties, and limitations 26:759–762

Mann ME, Zhang Z, Rutherford S, Bradley RS, Hughes MK, Shindell D, Ammann C, Faluvegi G, Ni F (2009) Global signatures and dynamical origins of the little ice age and medieval climate anomaly. Science 326(5957):1256–1260

Maxwell RS, Harley GL, Maxwell JT, Rayback SA, Pederson N, Cook ER, Barclay DJ, Li W, Rayburn JA (2017) An interbasin comparison of tree-ring reconstructed streamflow in the eastern united states. Hydrological processes 31(13):2381–2394

Maxwell RS, Belmecheri S, Taylor AH, Davis KJ, Ocheltree TW (2020) Carbon isotope ratios in tree rings respond differently to climatic variations than tree-ring width in a mesic temperate forest. Agricultural and Forest Meteorology 288:108014

McCarroll D, Pettigrew E, Luckman A, Guibal F, Edouard JL (2002) Blue reflectance provides a surrogate for latewood density of high-latitude pine tree rings. Arctic, Antarctic, and Alpine Research 34(4):450–453

McLaughlin S, Downing D, Blasing T, Cook E, Adams H (1987) An analysis of climate and competition as contributors to decline of red spruce in high elevation appalachian forests of the eastern united states. Oecologia 72(4):487–501

Melvin TM, Briffa KR (2008) A "signal-free" approach to dendroclimatic standardisation. Dendrochronologia 26(2):71–86

Overland J, Francis JA, Hall R, Hanna E, Kim SJ, Vihma T (2015) The melting arctic and midlatitude weather patterns: Are they connected? Journal of Climate 28(20):7917–7932

Patterson T, Maxwell RS, Harley GL, Oliver JS, Speer JH, Collins S, Downe M, Gannon B, Ma L, Raso C, et al. (2016) Climate—growth relationships of pinus rigida (mill.) at the species' northern range limit, acadia national park, me. Northeastern naturalist 23(4):490–500

Pearl JK, Anchukaitis KJ, Pederson N, Donnelly JP (2017) Reconstructing northeastern united states temperatures using atlantic white cedar tree rings. Environmental Research Letters 12(11):114012

Pearl JK, Anchukaitis KJ, Donnelly JP, Pearson C, Pederson N, Gaylord MCL, McNichol AP, Cook ER, Zimmermann GL (2020a) A late holocene subfossil atlantic white cedar tree-ring chronology from the northeastern united states. Quaternary Science Reviews 228:106104

Pearl JK, Anchukaitis KJ, Pederson N, Donnelly JP (2020b) Multivariate climate field reconstructions using tree rings for the northeastern united states. Journal of Geophysical Research: Atmospheres 125(1):e2019JD031619

Pederson N, Cook ER, Jacoby GC, Peteet DM, Griffin KL (2004) The influence of winter temperatures on the annual radial growth of six northern range margin tree species. Dendrochronologia 22(1):7–29

Rantanen M, Karpechko AY, Lipponen A, Nordling K, Hyvärinen O, Ruosteenoja K, Vihma T, Laaksonen A (2022) The arctic has warmed nearly four times faster than the globe since 1979. Communications Earth & Environment 3(1):168

Rayner N, Parker DE, Horton E, Folland CK, Alexander LV, Rowell D, Kent EC, Kaplan A (2003) Global analyses of sea surface temperature, sea ice, and night marine air temperature since the late nineteenth century. Journal of Geophysical Research: Atmospheres 108(D14)

Robeson SM, Maxwell JT, Ficklin DL (2020) Bias correction of paleoclimatic reconstructions: A new look at 1,200+ years of upper colorado river flow. Geophysical Research Letters 47(1):e2019GL086689

Sheppard PR, Graumlich LJ, Conkey LE (1996) Reflected-light image analysis of conifer tree rings for reconstructing climate. The Holocene 6(1):62–68

Stern RL, Schaberg PG, Rayback SA, Murakami PF, Hansen CF, Hawley GJ (2021) Eastern white pine and eastern hemlock growth: possible tradeoffs in response of canopy trees to climate. Canadian Journal of Forest Research 51(12):1926–1938

Tardif J, Brisson J, Bergeron Y (2001) Dendroclimatic analysis of Acer saccharum, Fagus grandifolia, and Tsuga canadensis from an old-growth forest, southwestern Quebec. Canadian Journal of Forest Research 31(9):1491–1501

Toohey M, Sigl M (2017) Volcanic stratospheric sulfur injections and aerosol optical depth from 500 bce to 1900 ce. Earth System Science Data 9(2):809–831

Trinies CA, Bunn AG, Robertson CS, Anchukaitis KJ (2022) Dendroclimatology of yellow-cedar (callitropsis nootkatensis) and temperature variability on the western slopes of the north cascades in washington state, usa, from 1333 to 2015 ce. Tree-Ring Research 78(2):113–128

Trouet V, Babst F, Meko M (2018) Recent enhanced high-summer north atlantic jet variability emerges from three-century context. Nature communications 9(1):180

Vose R, Easterling DR, Kunkel K, LeGrande A, Wehner M (2017) Temperature changes in the united states. Climate science special report: Fourth national climate assessment 1(GSFC-E-DAA-TN49028)

Wahl ER, Ammann CM (2007) Robustness of the Mann, Bradley, Hughes reconstruction of northern hemisphere surface temperatures: Examination of criticisms based on the nature and processing of proxy climate evidence. Climatic Change 85(1):33–69

Wang F, Arseneault D, Boucher É, Gennaretti F, Yu S, Zhang T (2022) Tropical volcanoes synchronize eastern canada with northern hemisphere millennial temperature variability. Nature Communications 13(1):5042

Wigley TML, Briffa KR, Jones PD (1984) On the average value of correlated time series, with applications in dendroclimatology and hydrometeorology. Journal of Climate and Applied Meteorology 23:201–213

Wiles G, Charlton J, Wilson RJ, DArrigo R, Buma B, Krapek J, Gaglioti BV, Wiesenberg N, Oelkers R (2019) Yellow-cedar blue intensity tree ring chronologies as records of climate, juneau, alaska, usa. Canadian Journal of Forest Research (ja)

Wilson R, D'Arrigo R, Buckley B, Büntgen U, Esper J, Frank D, Luckman B, Payette S, Vose R, Youngblut D (2007) A matter of divergence: tracking recent warming at hemispheric scales using tree ring data. Journal of Geophysical Research: Atmospheres 112(D17)

Wilson R, Anchukaitis K, Briffa KR, Büntgen U, Cook E, D'arrigo R, Davi N, Esper J, Frank D, Gunnarson B, et al. (2016) Last millennium Northern Hemisphere summer temperatures from tree rings: Part I: The long term context. Quaternary Science Reviews 134:1–18

Wilson R, Anchukaitis K, Andreu-Hayles L, Cook E, D'Arrigo R, Davi N, Haberbauer L, Krusic P, Luckman B, Morimoto D, et al. (2019) Improved dendroclimatic calibration using blue intensity in the southern Yukon. The Holocene 29(11):1817–1830

Zheng Y, Shen H, Abernethy R, Wilson R (2023) Experiments of the efficacy of tree ring blue intensity as a climate proxy in central and western china. Biogeosciences 20(16):3481–3490